EDGE ARTICLE

Nitrogen fixation using metallic lithium nanoparticles formed by electrospray deposition†

Dylan T. Holden, [ID] [a] Myles Quinn Edwards, [ID] [a] Zhongxia Shang [ID] [b]
and R. Graham Cooks [ID] *[a]

Multiphase reduction of ambient dinitrogen (N_2) was observed during the deposition of charged or uncharged aqueous microdroplets containing a lithium salt pre-catalyst onto conducting or inert surfaces to yield mixed lithium nanoparticles. We propose that this method leverages the high electric fields and partial solvation of ions at the gas–water–solid interface to enhance reaction rates and perform normally moisture-sensitive chemistry in aqueous droplets. Ammonia (NH_3) is formed and Li^+ is regenerated from the hydrolysis of transient lithium nitride Li_3N, constituting a complete catalytic cycle. The ammonia is captured *in situ* using formaldehyde to yield hexamethylenetetramine, a solid nitrogenous fuel. By measuring product formation with mass spectrometry, it was determined that 2.97 ± 0.36 µg h^{-1} of NH_3 was produced by a single spray source when using pure N_2 sheath gas and an applied potential, though microdroplets alone appear a sufficient source of electrons in cases where an external potential is not applied; air is also an adequate source of N_2 to produce NH_3. The mixed lithium metal nanoparticles were characterized with (S)TEM, EDS, and EELS. This ammonia synthesis has implications for the formation of nitrogenous compounds in environmental, prebiotic, and traditional synthetic contexts.

Introduction

Ammonia (NH_3) is among the most important of all commodity chemicals due to its use as fertilizer. It is primarily synthesized *via* the energy intensive and environmentally harmful Haber–Bosch (H–B) process where molecular nitrogen (N_2) and petroleum-derived hydrogen react under extreme temperatures (400–550 C) and pressures (150–300 atm) using fused-iron catalysts. This process consumes approximately 2% of the world's yearly fossil fuel energy output and generates over half a billion metric tons of carbon dioxide (CO_2) as a byproduct.[1-4] Despite nearly a century of research into scalable chemical and biological nitrogen fixation, Haber–Bosch still dominates industrial ammonia production, signifying a clear need for efficient and sustainable alternatives.[4-17]

While numerous methods exist for cleaving the highly stable N≡N triple bond (BDE 941 kJ mol^{-1}),[18] these typically require the use of toxic and/or costly transition metal catalysts.[19] Electrochemical strategies have been heralded as green alternatives to the H–B process due to the availability of less-toxic electrocatalysts, as well as the relative ease of scaling up such reactions.[20] Practical implementation of this approach has been limited due to competition with hydrogen evolution reactions and water

incompatibility. Several publications describe the use of 'physical catalysts' such as high local electric fields and the resulting ion chemistry that activates N_2 prior to reduction,[21] often utilizing water or H_2 as a proton source. Related examples include spontaneous aqueous electrochemical reduction at N-doped carbon nanospikes,[22] use of metal plasmas,[23,24] corona discharges in humid N_2-rich atmospheres,[25] contact electrification at hydrophobic interfaces,[26] as well as reactions at the charged gas–water–solid interfaces of aqueous microdroplets and iron catalysts.[27]

Recently, lithium-metal-based nitrogen fixation approaches have garnered attention due to the high speed and efficiency with which the corresponding nitride Li_3N can be formed under ambient conditions and subsequently reacted with water to yield NH_3 and regenerate Li^+ ions.[28,29] By spatially or temporally separating the processes of Li^+ reduction, Li metal nitridation, and Li_3N hydrolysis, it is possible to achieve efficient NH_3 production while retaining water as a proton source and potentially limiting unwanted H_2 production.[30] Further, lithium may also serve an alternative role in direct NH_3 production by enhancing electric field effects at sharp tips.[22]

Inspired by the discovery that microdroplets accelerate chemical reactions, largely *via* generation of reactive species and partial solvation of reagents at the spontaneously charged gas–liquid interface,[31-33] we explored the possibility that lithium-containing water microdroplets might be a viable strategy for rapid and sustainable small-scale NH_3 production. Taking advantage of the high concentration[34] and partial solvation of Li^+ ions at the (relatively) water-deficient surface[35] of the microdroplet, we

[a]Department of Chemistry, Purdue University, 560 Oval Dr, West Lafayette, IN 47907, USA. E-mail: cooks@purdue.edu

[b]Birck Nanotechnology Center, Purdue University, 1205 W State St, West Lafayette, IN 47907, USA

deposited droplets formed with or without an applied external potential to a grounded graphite counter electrode or a non-conductive surface to facilitate Li^+ reduction to Li^0. Simultaneous formation of mixed Li nanoparticles (Li NPs) on the deposition surfaces was observed. Electrospray deposition (ESD) is a widely utilized technique in industrial and academic contexts for preparing NPs and other nanostructured materials from polymers or metal salts, and their presence can increase the rates of heterogeneous reactions.[36–42] By carefully controlling the sheath gas and liquid flow rates, spray voltage, as well as the spray distance, it was possible to form Li NPs or Li dendrites at the cathode surface followed by reaction of N_2 (or compressed air) sheath gas with ambient water provided by the nearly de-solvated microdroplets to yield NH_3. Formaldehyde, added to the Li^+ solution, enabled in situ derivatization of produced ammonia via hexamethylenetetramine (hexamine) synthesis, a solid adamantine nitrogenous fuel of considerable industrial,[43–46] synthetic,[47] and prebiotic[48–53] relevance.

Results and discussion

Mechanistic investigation of ammonia synthesis via electrospray deposition

To examine the feasibility of reducing Li^+ in an aqueous ESD system, nano-electrospray (nESI) analysis was performed following cathodic ESD of a solution of 100 mM LiBr 3.7%

formaldehyde (v/v) with N_2 sheath gas, revealing a strong signal at m/z 141 attributed to protonated hexamine. Fig. 1A details the (electro)spray deposition apparatus and conditions utilized to perform the electrospray deposition and NH_3 trapping experiments. To verify the identity of the presumptive product (Fig. 2A), high-resolution mass spectrometry (HRMS) and tandem mass spectrometry (MS/MS) were performed on the surface wash solution following ESD. The elemental composition of the m/z 141 peak (Fig. S1†) is $C_6H_{13}N_4^+$, corresponding to protonated hexamine. Analysis of the product ion spectrum of hexamine reveals a series of neutral loss species with alternating mass differences of 13 and 14 Da (Fig. 2B). From precursor ion m/z 141 [hexamine + H]$^+$, the first neutral loss corresponds to methanimine (CH_2NH), giving a product ion at m/z 112. The remaining product ion peaks reveal neutral losses of C_2H_5N (m/z 98), $C_2H_4N_2$ (m/z 85), $C_3H_6N_2$ (m/z 71), and $C_3H_5N_3$ (m/z 58), corresponding to fragmentation events along the C–N backbone of hexamine. The identity of the product at m/z 141 formed following ESD was confirmed with a hexamine standard (Fig. S2†) and with previously reported hexamine MS/MS spectra.[48]

Lithium has been shown to assist in the synthesis of NH_3 from N_2 through at least two mechanisms: via a Li_3N intermediate or through enhancement of local electric fields, the latter allowing for activation and direct electrolysis of the N≡N triple bond in aqueous systems.[22,28] Previous work has described a cation size effect on the rate of aqueous NH_3 production at N-
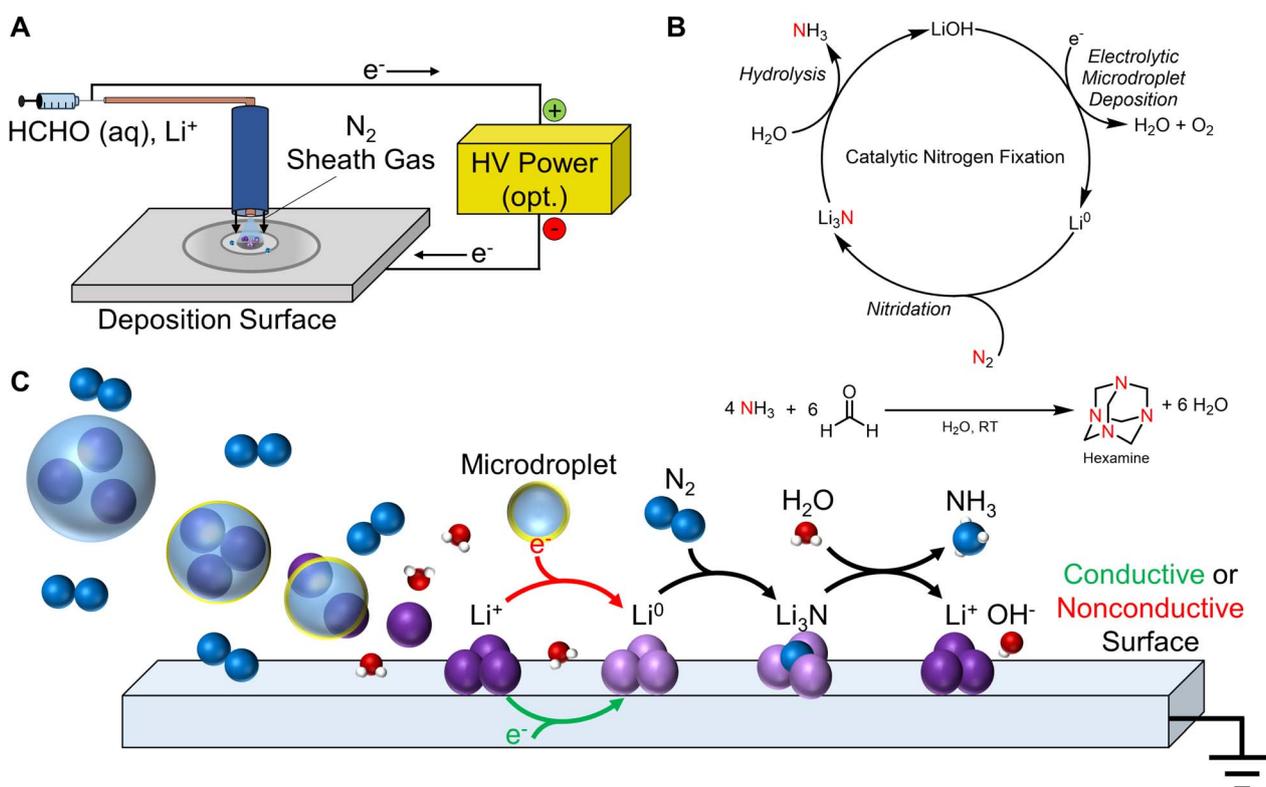

Fig. 1 (A) Schematic of the general (electro)spray deposition apparatus utilized in this study. Application of an external potential is optional. (B) Catalytic electrochemical cycle proposed as the primary mechanism of nitrogen fixation when performing ESD of aqueous lithium solutions (top) with in situ ammonia capture by formaldehyde to yield hexamine (bottom). (C) Pictorial representation of the ESD-mediated formation of lithium nanoparticles and associated electrochemical nitrogen fixation to yield ammonia. Single-electron reduction of Li^+ is proposed to occur via electron transfer from a conductive surface or upon microdroplet collision in the absence of an externally applied potential.
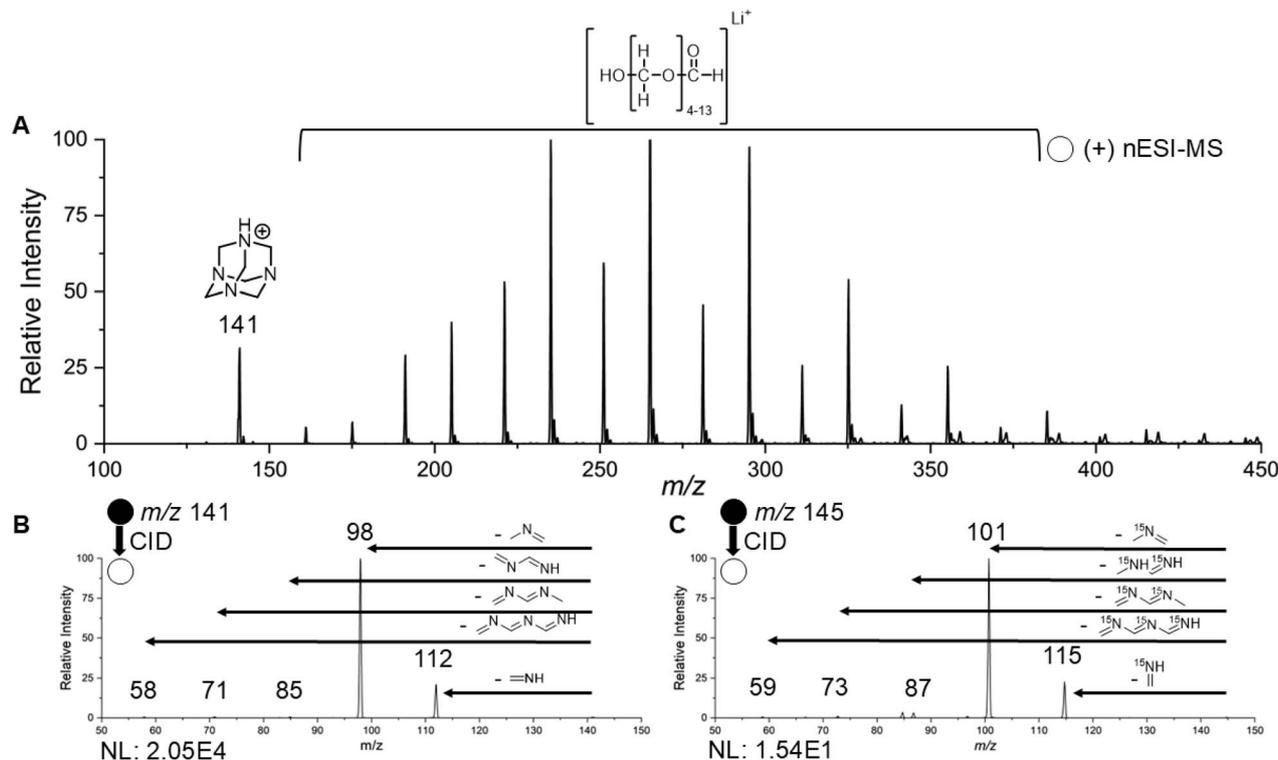
Fig. 2 (A) Full scan mass spectrum following ESD of a LiBr and formaldehyde solution for 60 minutes with N_2 sheath gas showing the protonated hexamine product (m/z 141) and a polymeric distribution attributed to lithium-adducted paraformaldehyde-related species. (B) MS/MS spectrum of the peak in (A) observed at m/z 141. (C) MS/MS spectrum following similar ESD conditions to those in (A) but with ^{15}N-labeled N_2 mixed with pure N_2 sheath gas (10% v/v).

doped carbon nanospikes ($Li^+ > Na^+ > K^+$), where the smaller Li^+ ions might provide a greater charge density at the nanospike tip while also limiting access of water to the Stern layer where N_2 reduction occurs.[22] Given that microdroplets inherently possess large interfacial electric fields,[54,55] even in the absence of an externally applied potential, various alkali bromide salts were screened to examine their effect on NH_3 production via local field enhancement. NaBr and KBr were added to formaldehyde solutions and, despite extensive effort at optimizing the ESD conditions, the hexamine product was undetectable by MS in all cases (Table S3†). This suggests that NH_3 is formed via the hydrolysis of transient Li_3N rather than through direct N_2 activation by a cation-augmented electric field (Fig. 1B). Further description of the electrochemical half-cell reactions is detailed in Scheme S1.† While alignment and activation of N_2 might still occur at the surface of the microdroplet's air–water interface, this alone cannot explain the observed ammonia production.

To probe Li_3N involvement, various lithium salts were screened for their ability to produce NH_3. Of the three salts examined, LiBr and $LiClO_4$ produced similar amounts of hexamine after 20 minutes of deposition, with a thin and evenly distributed white coating of LiBr and polymerized formaldehyde (paraformaldehyde), as well as faint some faint brown-orange material (Li_3N) on the graphite surface (Fig. S3A†). However, ESD of a 100 mM LiOH and formaldehyde solution resulted in the formation of macroscopic tower-like structures (Fig. S3B†) that, when dissolved in water, yielded a detectable but significantly

lower intensity hexamine signal. This observation is presumably due to rapid base-catalyzed polymerization of formaldehyde to paraformaldehyde,[56] which formed in the LiBr and $LiClO_4$ solutions, but is of considerably lower concentration due to neutralization of any LiOH by strong conjugate acids HBr and $HClO_4$, respectively. The observed selectivity of hexamine formation with inclusion of only Li-containing salts implicates the involvement of Li^0 and Li_3N as reactive intermediates in this method. Note that it might also be possible for formaldehyde to react directly with Li_3N to form hexamine, though investigation of this secondary mechanism is beyond the scope of this study.[57]

To control for environmental NH_3 contamination and demonstrate N≡N bond cleavage, the N_2 sheath gas stream was diluted 10% with compressed ^{15}N-labeled N_2 and the ESD experiment was performed as previously described. Peaks corresponding to multiple ^{15}N incorporation events are observed in the high-resolution full scan mass spectrum, largely favoring the incorporation of 1–2 ^{15}N atoms, supporting the argument that this method primarily utilizes N_2 as the nitrogen feedstock (Table S1, Fig. S4A and B†). While instrument contamination reduced the quality of the high-resolution MS/MS spectrum of m/z 145 (Fig. S4C†), the low-resolution mass spectrometer did not show signs of contamination (Table S2†) and the tetrasubstituted product at m/z 145 could be isolated and subject to MS/MS (Fig. 2C); the resulting product ions correspond well with the mass shifts expected when compared to those of unlabeled hexamine at m/z 141 (cf. Fig. 2B).

Quantitation of NH_3 production in charged and uncharged droplet systems

While the inherent electric field at the gas–water interface does not appear to be sufficient for direct electrolysis of N_2 (at least in quantities capable of determination by MS on this limited timescale), the surface charge layer might still contribute to the reduction of surface Li^+ in instances when an external potential is not applied (and when a nonconductive surface is used). To investigate this possibility, a calibration curve was constructed to quantify the amount of hexamine produced under various deposition conditions (Fig. 3A). Standard ESD conditions using LiBr as the electrolyte with a positive charge applied to the metal syringe needle and a grounded graphite surface resulted in an average rate of 2.97 ± 0.36 μg NH_3 per hour per sprayer with an RSD of 8.7% as determined by the original peak ratios and hexamine concentration (Fig. 3A, blue data point), as determined by the observed hexamine yield (see ESI,† Methods and materials). This value of 2.97 ± 0.36 μg NH_3 per hour per sprayer is approximately 4 times greater than previously reported microdroplet or electrospray-related ammonia formation methodologies.[25,27] Changing the electrolyte from LiBr to $LiClO_4$ returned a similar rate of ammonia production (Table S2†), demonstrating no significant counterion effect. Note that all reported values are likely underestimates given that MS detection is dependent on capture of NH_3 by formaldehyde, an undoubtedly inefficient process given the volatility of both the formaldehyde and the NH_3 in conjunction with the pneumatic force of the surrounding sheath gas.

When the external spray potential was removed, the rate of NH_3 production decreased to approximately 320 ± 220 ng per hour per sprayer (Fig. 3A, green data point). This value was remarkably constant across trials where a potential was not applied to graphite and in those where a non-conductive surface such as Parafilm was used (Fig. S5†). The RSD for this point falls between the limit of quantitation and the limit of detection so, while this value is consistent across trials and conditions, one cannot compare it directly to the high voltage NH_3 yield. This suggests that while it is certainly more efficient for Li^+ to be reduced at a negatively biased conductive surface, it is still possible for transient Li metal to form from spray deposition alone. Surface effects in aqueous microdroplets, such as partial solvation, can produce strong reducing agents[58–60] (e.g. hydrated electrons[61–64]) and enable redox chemistry normally prohibited in bulk solution. We propose that electrons with a sufficiently high electrochemical potential can be primed and transferred to the deposited Li^+ ion from impinging charged droplets to perform single-electron reduction and form highly reactive Li metal (Fig. 1C).

Additional considerations

A peak at m/z 141 is often observed even in cases where formaldehyde is not included (Fig. S6A†). This species, identified as lithium-adducted diethylene glycol monoethyl ether (DEGMEE), has previously been reported as a ubiquitous contaminant in ambient ionization experiments.[65] Given that this species can be differentiated from protonated hexamine (also at m/z 141) in unit-resolution MS experiments via MS/MS (Fig. S6B†), simultaneous quantitation of hexamine (and thus NH_3) yields and contaminant abundance were performed by employing a wide-isolation window MS/MS method (see ESI,† Methods and materials for more information on this strategy of quantitation).

Paraformaldehyde formation is present in all ESD experiments which include formaldehyde, as evidenced by
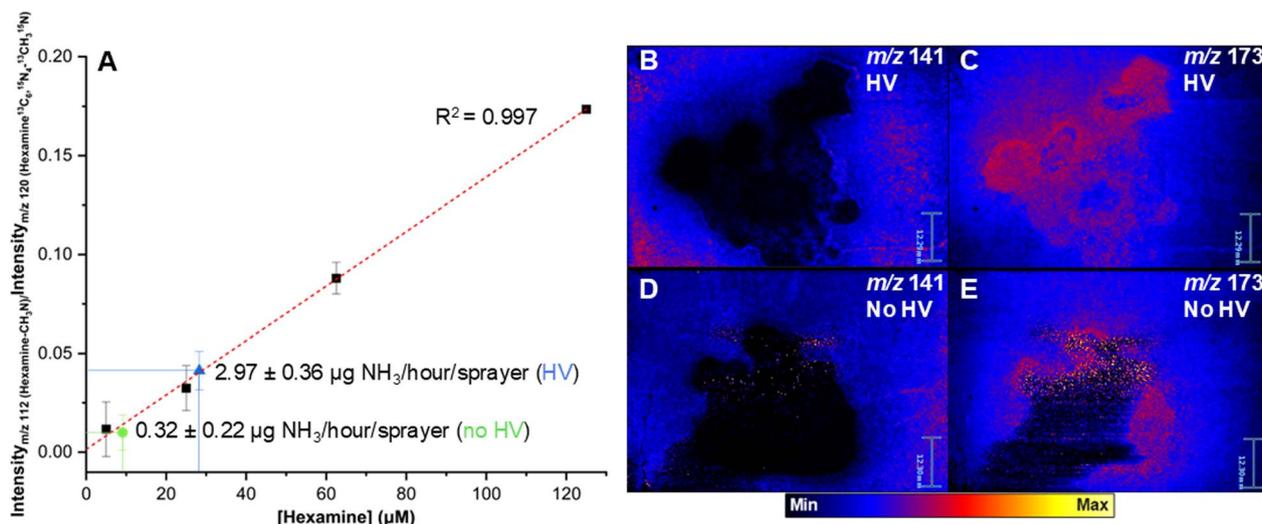

Fig. 3 (A) Calibration curve constructed to determine the approximate rate of NH_3 production across various experimental conditions. The blue extrapolated point refers to the average hexamine concentration found after washing a graphite surface following electrospray deposition of the LiBr and formaldehyde solution used in Fig. 2, whereas the green point corresponds to the same experiment albeit without an applied potential. (B–E) DESI-MS ion images of two separate graphite surfaces following 20-minute deposition experiments. (B) and (C) Show the distribution of protonated hexamine (m/z 141) and the lithium adduct of a paraformaldehyde unit (m/z 173) with a potential applied to the spray apparatus and a grounded graphite surface. (D) and (E) Show the distribution of the same two species without an externally applied potential. The signals for each pair of images (B–E) are normalized to the total ion current from each round of imaging and the scale bar is 12.30 mm.

a polymeric distribution of peaks from *ca. m/z* 150–400 in the corresponding mass spectra (Fig. 2A; not observed with direct nESI of the reaction solution (Fig. S7†)). Assuming Li^+ reduction primarily occurs at the electrode surface (though not exclusively, as demonstrated previously) and that the resulting Li^0 must contact N_2 gas to form the corresponding nitride, the continuous vertical deposition of hydrated paraformaldehyde inhibits both of these processes through blocking of the surface as well as any transiently formed Li_3N, deceasing hexamine yields over time.

The reduced hexamine yields on the deposition surface can be visualized by desorption electrospray ionization mass spectrometry (DESI-MS) imaging of the graphite surface before (Fig. S8C†) and after (electro)spray deposition (Fig. 3B–E). The ion [hexamine + H]$^+$ gives strong signals along the periphery of the deposition area. The distribution of paraformaldehyde (selected peak at *m/z* 173, $[C_5H_{10}O_6 + Li]^+$) is effectively the opposite of that observed for hexamine. The highest intensity signals for paraformaldehyde occur in the middle of the deposition surface, centered on the most direct point of contact of the spray plume. When the spray potential is removed, the overall hexamine abundance is decreased relative to the total ion current for each set of DESI-MS images.

Thin films, contaminant control, and NH_3 production from air

Li metal is highly reactive both with water and O_2, thus necessitating the use of spray methods and a protective sheath gas to place reagents at the 'dry' air–water interface[35] and to prevent significant accumulation of water on the deposition surface, respectively. To verify the role of microdroplets in this reduction, solutions of pure water, aqueous formaldehyde, aqueous LiBr, and the formaldehyde/LiBr reaction mixture were directed onto a grounded graphite surface using the standard ESD parameters albeit with a significantly increased solution flow rate (250 μL min^{-1}, an order of magnitude faster than in the standard ESD experiments to minimize microdroplet formation) in the absence of a sheath gas. Solutions were then spread radially across the surface to produce thin films and an N_2 gas flow was directed from above to ensure contact with the thin films. After 3 hours, the dried surfaces were washed and analyzed by nESI-MS. Hexamine was not detected from any of the solutions (Fig. S9A–D†). Thin films have been shown to serve as high surface-to-volume ratio systems that retain some aspects of the increased reactivity observed for microdroplets, thus this result highlights the importance of spray deposition and droplet evaporation in performing moisture-sensitive chemistry from an aqueous parent solution.

Given that indoor NH_3 concentrations can reach upwards of 1 part per million[66,67] and that NH_3 has been reported as a contaminant in some compressed gas cylinders,[68] a more detailed inquiry into the origin of the nitrogen fixed during the spray deposition experiments beyond the already mentioned isotope labeling experiment was performed. As a precaution, all spray deposition experiments were performed inside of a fume hood to minimize the potential impact of ambient

contaminants. To determine whether the compressed N_2 or Ar tanks contained any trace NH_3, the gases were bubbled through a solution of formaldehyde and LiBr, similar to that used in the spray deposition experiments. After two hours of bubbling with either gas, the reaction mixtures were directly analyzed by MS and no signals which might correspond to protonated hexamine were observed (Fig. S10A and B†); this further reinforces the null results found for the thin film control experiments (Fig. S9A–D†). Ar gas was used when depositing standard solutions used in constructing the calibration curve shown previously (Fig. 3A). The procedure was repeated with compressed laboratory air from outside the fume hood which resulted in a low intensity signal matching that of hexamine (Fig. S10D†), suggesting that ambient laboratory NH_3 could be a source of error if introduced into the fume hood. However, bubbling compressed laboratory air from inside of the fume hood did not yield any hexamine product (Fig. S10C†), likely due to limited introduction and efficient ventilation of NH_3. Neither contaminant NH_3 in the gas cylinders nor ambient NH_3 from outside the fume hood were indicated to play a significant role in the reported nitrogen fixation.

Knowing that compressed laboratory air from inside the fume hood is not a significant source of NH_3, we investigated whether air could be used as a convenient source of N_2 for Li-mediated NH_3 production. After 60 minutes of ESD using compressed laboratory fume hood air as the sheath gas, a detectable hexamine peak was observed in the corresponding mass spectrum (Fig. S11†). It should be noted that the significant decrease in the hexamine peak intensity relative to the paraformaldehyde peaks compared to that in Fig. 2A (pure N_2) can be explained both by the *ca.* 20% decrease in total N_2 in ambient air in addition to the consumption of Li metal and Li_3N *via* reaction with O_2 and H_2O.

Li nanoparticle synthesis and characterization

Heterogeneous reactions are generally accelerated as catalytic particle size decreases due to the increased availability of active surface sites relative to the total amount of catalyst.[69] Given that ESD of metal salts often results in formation of metal nanoparticles,[40] we investigated whether Li NPs (*e.g.* Li^0, Li_3N, Li_2O) form during our ESD experiments which might further accelerate surface chemistry, outcompeting hydrolysis.

Transmission electron microscopy (TEM) analysis was performed following nano-electrospray ESD of the formaldehyde/LiBr solution onto a grounded Cu TEM grid. As evident in Fig. 4A and B, spheroidal NPs formed with an average diameter of 8.44 ± 2.24 nm and a polydispersity index of 0.07, indicating a highly monodispersed population.[70] An additional population of larger cubic particles was also observed (Fig. 4A, inset top). When the spray voltage was increased to 3 kV, dendritic species were formed upon deposition rather than NPs (Fig. 4A, inset bottom). Energy-dispersive X-ray spectroscopy (EDS) of an area similar to Fig. 4A (though also including cubic particles) revealed unique atomic signatures corresponding to Br and N (Fig. 3C), which were not observed for the blank TEM grid (Fig. S12†). Scanning transmission electron micrscopy
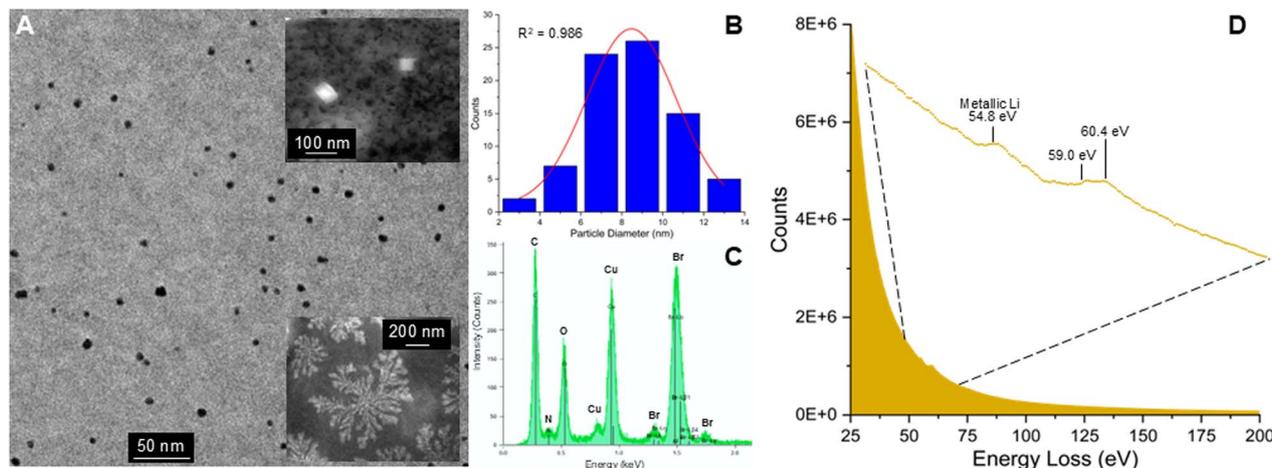
Fig. 4 (A) TEM micrograph of Li- and N-containing nanoparticles formed *via* electrospray deposition with (inset, top) STEM micrograph of larger cubic Li/LiBr/Li$_2$O$_x$/LiOH particles observed within the same population. Increasing the spray potential to from 2 kV to 3 kV resulted in the formation of Li/Li$_2$O$_x$ dendrites rather than NPs (inset, bottom). (B) Associated particle size distribution (average dia. $= 8.44 \pm 2.24$ nm) for those shown in A. (C) EDS spectrum detailing the atomic composition of the nanoparticles in A. Cu, C, and a portion of the O signatures arise from the Formvar-coated Cu TEM grid. Br signatures primarily arise from the larger cubic NPs while N are primarily observed in the smaller spheroidal NPs. (D) EELS analysis of a separate albeit similar nanoparticle population as that in (A) deposited under ambient conditions. Peaks with energy-loss threshold values corresponding to metallic Li, lithium halides, and/or lithium oxides are evident.

(STEM) combined with EDS showed that the cubic structures primarily consist of Br and O (Fig. S13D and E†). STEM-EDS imaging revealed the increased presence of nitrogen in areas the smaller spheroidal NPs reside (Fig. S13C†). This, in conjunction with the overall average increase in N-related EDS signals with both LiBr and LiBr/HCHO compared to a blank TEM grid (Fig. S12†), suggests that Li$_3$N is formed during this experiment and is present in the smaller spheroidal NPs. Li metal is likely present in the area analyzed, though traditional EDS is insensitive to the low-energy X-rays characteristic of Li.[71]

To directly confirm the presence of metallic Li in the observed NPs, electron energy loss spectroscopy (EELS) was performed given its sensitivity to light elements.[72] As shown in Fig. 4D, the K-edge for metallic Li can be directly observed with a peak at a threshold energy loss value of *ca.* 54.8 eV, in agreement with previously reported values.[73] An additional set of peaks can be observed at 59.0 eV and 60.4 eV. While interpretation of the fine structure of these peaks is difficult due to the intensity of the plasmon peak spanning 25–200 eV, the threshold values and peak shapes resemble to those previously found for LiOH, Li halides (LiBr in this case), Li$_2$O$_x$, and LiOH.[73–75] Elemental mapping of the EELS spectra to an STEM image reveals that metallic Li and oxygen are primarily localized in the cubic NPs, while lower densities are observed in the surrounding paraformaldehyde films and smaller spheroidal NPs (Fig. S14A–D†). Similarly, EELS confirmed the dendritic species shown in the bottom inset panel of Fig. 4A primarily consist of metallic Li and Li$_2$O$_x$ (Fig. S15†). These dendrites, the formation of which is of major concern in Li-based batteries,[76] might prove to be advantageous in terms of heterogeneous catalysis (as described in this manuscript) due to the greater surface area compared to spheroidal or cubic NPs.

The presence of lithium oxides is further substantiated by nESI-MS analysis of the deposited LiBr/HCHO solution. Compared to the original bulk LiBr solution (Fig. S16A†), this sample revealed increased formation of small LiBr/Li$_2$O$_x$/LiOH clusters (Fig. S16B†) and is likely representative of initial clustering events leading to the cubic NPs. No pure or mixed metallic Li clusters were observed by MS, likely due to the reconstitution of the NPs in water prior to nESI analysis. Together, these data suggest that the cubic NPs likely consist of both LiBr, Li$_2$O, Li$_2$O$_2$, and LiOH.

The formation of Li NPs with large surface area likely facilitates the observed NH$_3$ production *via* accelerated Li$_3$N formation, outcompeting reactions with water from the spray. Paraformaldehyde formed *in situ* may also contribute to Li NP stability by providing a water deficient protective coating. To this point, the abundance of NPs observed with the inclusion of HCHO generally appeared to be significantly greater than without. To the authors' knowledge this is the first example of mixed Li/LiBr/Li$_2$O$_x$/LiOH/Li$_3$N NP synthesis *via* ESD. Li NPs have garnered attention for their distinctive qualities as electrodes and additives for lithium-ion and lithium–air batteries and hence this approach might also represent a feasible strategy for novel materials preparation.[77,78]

Conclusions

With atmospheric CO$_2$ levels at climate-altering levels and a lack of widespread sustainable energy and NH$_3$ sources, deployment of environmentally sustainable strategies to the Haber–Bosch process are imperative, even if initially made on a small scale; they include the catalytic lithium-mediated NH$_3$ cycle shown here. The ambient water microdroplet serves as a reaction vessel that contains the proton source, the electron source (in the case of deposition onto non-conducting surfaces), and it provides a means for generating metal nanoparticles upon surface collisions. The multifunctionality of the

demonstrated microdroplet chemistry has potential to lessen the environmental and economic burden that the use of conventional solvents, extreme reaction environments, and the generation of H_2 gas from fossil fuels normally entail. We also demonstrate rapid *in situ* capture of transient NH_3 with simple and inexpensive reagents in the spray solution to form hexamine without need to access high temperatures or pressures.

These results add to growing evidence that the air–water interface of microdroplets is effectively water-deficient and may serve as a means of performing water-sensitive reactions in aqueous systems. The successful generation of Li metal NPs in an aqueous system shown here is largely made possible through the combination of primed reagents at the microdroplet interface reacting with gas–solid nanoparticle surfaces. We envision that similar reaction formats will enable a new branch of green synthesis for condensation reactions, organometallic reactions, electrochemical processes, and might also serve as laboratory models for multiphase prebiotic chemistry. Furthermore, the role of charged microdroplet collisions with solid surfaces is demonstrated by the generation of NH_3 without the need for application of an external potential or a conductive deposition surface, a seldom explored possibility in previous electrospray deposition studies. Similar chemistry has recently been highlighted by Pradeep and coworkers as a potentially major source of spontaneous mineral weathering in nature.[79]

This method's relatively rapid rate of NH_3 production compared to other reported microdroplet syntheses can be attributed to both the general speed of Li_3N formation and hydrolysis, as well as the presence of Li NPs formed during the spray deposition process. The inclusion of protecting ligands in the Li salt solution might increase the lifetime of the Li NPs by shielding them from water, allowing for additional NH_3-capture reactions to be implemented. Methods of multiplexing sprayers, solvent recycling,[80] continuous surface de-fouling, improved reactor design, as well as direct ammonia condensation could also be employed to increase yields and further assist scaling up of the microdroplet deposition process. With these modifications, this system has the potential to be a valuable method of generating preparative amounts of NH_3 from pure N_2 or air for use in as a bulk chemical or in organic synthesis, utilizing minimal resources in the process.

Data availability

All data on which this publication is based appears either in the main text or in the ESI.† The underlying raw data is available on request to the authors.

Author contributions

All authors contributed to experimental design and data interpretation. DTH and MQE performed TEM and MS experiments. ZS performed all STEM, EDS, and EELS experiments with contributions by DTH and MQE. DTH, MQE, and RGC wrote the manuscript.

Conflicts of interest

There are no conflicts to declare.

Acknowledgements

Notes and references

1 L. Wang, M. Xia, H. Wang, K. Huang, C. Qian, C. T. Maravelias and G. A. Ozin, *Joule*, 2018, **2**, 1055–1074.

2 C. Smith, A. K. Hill and L. Torrente-Murciano, *Energy Environ. Sci.*, 2020, **13**, 331–344.

3 S. Ghavam, M. Vahdati, I. A. G. Wilson and P. Styring, *Front. Energy Res.*, 2021, **9**, 1–19.

4 M. A. Nawaz, R. Blay-Roger, M. Saif, F. Meng, J. González-Arias, B. Miao, L. F. Bobadilla, T. Ramirez-Reina and J. A. Odriozola, *ACS Catal.*, 2023, **13**, 14415–14453.

5 D. Chanda, R. Xing, T. Xu, Q. Liu, Y. Luo, S. Liu, R. A. Tufa, T. H. Dolla, T. Montini and X. Sun, *Chem. Commun.*, 2021, **57**, 7335–7349.

6 A. J. Martín, T. Shinagawa and J. Pérez-Ramírez, *Chem*, 2019, **5**, 263–283.

7 S. L. Foster, S. I. P. Bakovic, R. D. Duda, S. Maheshwari, R. D. Milton, S. D. Minteer, M. J. Janik, J. N. Renner and L. F. Greenlee, *Nat. Catal.*, 2018, **1**, 490–500.

8 Y. Abghoui, S. B. Sigtryggsson and E. Skúlason, *ChemSusChem*, 2019, **12**, 4265–4273.

9 B. M. Hoffman, D. Lukoyanov, Z. Y. Yang, D. R. Dean and L. C. Seefeldt, *Chem. Rev.*, 2014, **114**, 4041–4062.

10 H. Himmel and M. Reiher, *Angew. Chem., Int. Ed.*, 2006, **45**, 6264–6288.

11 S. Reichle, M. Felderhoff and F. Schüth, *Angew. Chem., Int. Ed.*, 2021, **60**, 26385–26389.

12 D. Ziegenbalg, J. Zander and R. Marschall, *ChemPhotoChem*, 2021, **5**, 792–807.

13 T. Dai, T. Wang, Z. Wen and Q. Jiang, *Adv. Funct. Mater.*, 2024, 2400773.

14 S. Bennaamane, B. Rialland, L. Khrouz, M. Fustier-Boutignon, C. Bucher, E. Clot and N. Mézailles, *Angew. Chem., Int. Ed.*, 2023, **62**, e202209102.

15 T. Wang and F. Abild-Pedersen, *Proc. Natl. Acad. Sci. U.S.A.*, 2021, **118**, 1–5.

16 W. Qiu, X. Xie, J. Qiu, W. Fang, R. Liang, X. Ren, X. Ji, G. Cui, A. M. Asiri, G. Cui, B. Tang and X. Sun, *Nat. Commun.*, 2018, (9), 3485.

17 E. Spatolisano and L. A. Pellegrini, *Chem. Eng. Res. Des.*, 2023, **195**, 651–661.

18 P. Wang, S. Gong, Y. Li and Y. Mo, *J. Chem. Phys.*, 2024, **160**, 014304.

19 R. Akter, S. S. Shah, M. A. Ehsan, M. N. Shaikh, M. H. Zahir, M. A. Aziz and A. J. S. Ahammad, *Chem.–Asian J.*, 2024, **19**, e202300797.

20 S. C. Jesudass, S. Surendran, J. Y. Kim, T. Y. An, G. Janani, T. H. Kim, J. K. Kim and U. Sim, *Electrochem. Energy Rev.*, 2023, **6**, 27.

21 A. I. Gerasimchuk and D. A. Zhogolev, *Theor. Exp. Chem.*, 1977, **13**, 5–9.

22 Y. Song, D. Johnson, R. Peng, D. K. Hensley, P. V. Bonnesen, L. Liang, J. Huang, F. Yang, F. Zhang, R. Qiao, A. P. Baddorf, T. J. Tschaplinski, N. L. Engle, M. C. Hatzell, Z. Wu, D. A. Cullen, H. M. Meyer, B. G. Sumpter and A. J. Rondinone, *Sci. Adv.*, 2018, **4**, 1–8.

23 C. Geng, J. Li, T. Weiske and H. Schwarz, *Proc. Natl. Acad. Sci. U. S. A.*, 2019, **116**, 21416–21420.

24 C. Geng, J. Li, T. Weiske and H. Schwarz, *Proc. Natl. Acad. Sci. U. S. A.*, 2018, **115**, 11680–11687.

25 X. Gong, L. Feng, S. Tan, S. Cheng, R. Zhai, T. Peng, Y. Jiang, X. Dai, Y. Pan and X. Fang, *ACS Energy Lett.*, 2024, **9**, 2153–2161.

26 J. Li, Y. Xia, X. Song, B. Chen and R. N. Zare, *Proc. Natl. Acad. Sci. U. S. A.*, 2024, **121**(4), e2318408121.

27 X. Song, C. Basheer and R. N. Zare, *Proc. Natl. Acad. Sci. U. S. A.*, 2023, **120**, e2301206120.

28 N. Lazouski, Z. J. Schiffer, K. Williams and K. Manthiram, *Joule*, 2019, **3**, 1127–1139.

29 N. Futamura, T. Ichikawa, N. Imanishi, Y. Takeda and O. Yamamoto, *ECS Meet. Abstr.*, 2012, 1137.

30 J. M. McEnaney, A. R. Singh, J. A. Schwalbe, J. Kibsgaard, J. C. Lin, M. Cargnello, T. F. Jaramillo and J. K. Nørskov, *Energy Environ. Sci.*, 2017, **10**, 1621–1630.

31 X. Yan, R. M. Bain and R. G. Cooks, *Angew. Chem., Int. Ed.*, 2016, **55**, 12960–12972.

32 Z. Wei, Y. Li, R. G. Cooks and X. Yan, *Annu. Rev. Phys. Chem.*, 2020, **71**, 31–51.

33 T. Majumder, D. B. Eremin, B. Delibas, A. Sarkar, V. Fokin and J. M. Dawlaty, *Angew. Chem., Int. Ed.*, 2024, e202414746.

34 V. Kwan and S. Consta, *J. Am. Soc. Mass Spectrom.*, 2021, **32**, 33–45.

35 D. T. Holden, N. M. Morato and R. G. Cooks, *Proc. Natl. Acad. Sci. U. S. A.*, 2022, **119**, 1–8.

36 J. K. Lee, D. Samanta, H. G. Nam and R. N. Zare, *Nat. Commun.*, 2018, **9**, 1562.

37 S. Zhang and K. Kawakami, *Int. J. Pharm.*, 2010, **397**, 211–217.

38 A. Jana, S. K. Jana, D. Sarkar, T. Ahuja, P. Basuri, B. Monday, S. Bose, J. Ghosh and T. Pradeep, *J. Mater. Chem. A*, 2019, **7**, 6387–6394.

39 T. Ahuja, A. Ghosh, S. Mondal, P. Basuri, S. K. Jenifer, P. Srikrishnarka, J. S. Mohanty, S. Bose and T. Pradeep, *Analyst*, 2019, **144**, 7412–7420.

40 J. Ghosh and R. G. Cooks, *ChemPlusChem*, 2022, **87**, e202200252.

41 J. Ghosh and R. G. Cooks, *Trends Anal. Chem.*, 2023, **161**, 117010.

42 A. Li, Q. Luo, S. J. Park and R. G. Cooks, *Angew. Chem., Int. Ed.*, 2014, **53**, 3147–3150.

43 F. Meissner, E. Schwiedessen and D. F. Othmer, *Ind. Eng. Chem.*, 1954, **46**, 724–727.

44 T. S. Lo, K. D. P. Hammer, M. Zegarra and W. C. Cho, *Expert Rev. Anti-Infect. Ther.*, 2014, **12**, 549–554.

45 P. Roose, K. Eller, E. Henkes, R. Rossbacher and H. Höke, in *Ullmann's Encyclopedia of Industrial Chemistry*, 2015, pp. 1–55.

46 A. Alamdari and F. Tabkhi, *Chem. Eng. Process.*, 2004, **43**, 803–810.

47 N. Blažević, D. Kolbah, B. Belin, V. Šunjić and F. Kajfež, *Synthesis*, 1979, **3**, 161–176.

48 Y. Oba, Y. Takano, H. Naraoka, Y. Furukawa, D. P. Glavin, J. P. Dworkin and S. Tachibana, *Nat. Commun.*, 2020, **11**, 1–8.

49 V. Vinogradoff, S. Bernard, C. Le Guillou and L. Remusat, *Icarus*, 2018, **305**, 358–370.

50 C. He, G. Lin and M. A. Smith, *Icarus*, 2012, **220**, 627–634.

51 A. Zeffiro, S. Lazzaroni, D. Merli, A. Profumo, A. Buttafava, N. Serpone and D. Dondi, *Origins Life Evol. Biospheres*, 2016, **46**, 223–231.

52 H. Cottin, S. Bachir, F. Raulin and M. C. Gazeau, *Adv. Space Res.*, 2002, **30**, 1481–1488.

53 D. P. Glavin, J. P. Dworkin, M. O. Alexander, J. C. Aponte, A. A. Baczynski, J. J. Barnes, H. A. Bechtel, E. L. Berger, A. A. Burton, P. Caselli, A. H. Chung, S. J. Clemett, G. D. Cody, G. Dominguez, J. E. Elsila, K. K. Farnsworth, D. I. Foustoukos, K. H. Freeman, Y. Furukawa, Z. Gainsforth, H. V. Graham, T. Grassi, B. M. Giuliano, V. E. Hamilton, P. Haenecour, P. R. Heck, A. E. Hofmann, C. H. House, Y. Huang, H. H. Kaplan, L. P. Keller, B. Kim, T. Koga, M. Liss, H. L. McLain, M. A. Marcus, M. Matney, T. J. McCoy, O. M. McIntosh, A. Mojarro, H. Naraoka, A. N. Nguyen, M. Nuevo, J. A. Nuth III, Y. Oba, E. T. Parker, T. S. Peretyazhko, S. A. Sandford, E. Santos, P. Schmitt-Kopplin, F. Seguin, D. N. Simkus, A. Shahid, Y. Takano, K. L. Thomas-Keprta, H. Tripathi, G. Weiss, Y. Zheng, N. G. Lunning, K. Righter, H. C. Connolly Jr and D. S. Lauretta, *Nat. Astron.*, 2025, **9**, 199–210.

54 H. Hao, I. Leven and T. Head-Gordon, *Nat. Commun.*, 2022, **13**, 1–8.

55 H. Xiong, J. K. Lee, R. N. Zare and W. Min, *J. Phys. Chem. Lett.*, 2020, **11**, 7423–7428.

56 N. Brown, *J. Macromol. Sci., Part A: Pure Appl. Chem.*, 1967, **1**, 209–230.

57 J. M. Morris, R. B. Dunmire, P. E. Koenig and G. R. Newkome, *J. Org. Chem.*, 1972, **37**, 1244–1248.

58 Q. Liang, C. Zhu and J. Yang, *J. Am. Chem. Soc.*, 2023, **145**, 10159–10166.

59 L. Qiu and R. G. Cooks, *Angew. Chem., Int. Ed.*, 2024, **63**(17), e202400118.

60 M. Mofidfar, M. A. Mehrgardi and R. N. Zare, *Proc. Natl. Acad. Sci. U. S. A.*, 2024, **121**, e2315940121.

61 M. Armbruster, H. Haberland and H.-G. Schindler, *Phys. Rev. Lett.*, 1981, **47**, 323–326.

62 F. Arnold, *Nature*, 1981, **294**, 732–733.

63 W. A. Maza, V. M. Breslin and J. C. Owrutsky, *Curr. Opin. Chem. Eng.*, 2024, **44**, 101015.

64 J. K. Lee, D. Samanta, H. G. Nam and R. N. Zare, *J. Am. Chem. Soc.*, 2019, **141**, 10585–10589.

65 S. R. Kumbhani, L. M. Wingen, V. Perraud and B. J. Finlayson-Pitts, *Rapid Commun. Mass Spectrom.*, 2017, **31**, 1659–1668.

66 M. Li, C. J. Weschler, G. Bekö, P. Wargocki, G. Lucic and J. Williams, *Environ. Sci. Technol.*, 2020, **54**, 5419–5428.

67 L. Ampollini, E. F. Katz, S. Bourne, Y. Tian, A. Novoselac, A. H. Goldstein, G. Lucic, M. S. Waring and P. F. Decarlo, *Environ. Sci. Technol.*, 2019, **53**, 8591–8598.

68 R. Dabundo, M. F. Lehmann, L. Treibergs, C. R. Tobias, M. A. Altabet, P. H. Moisander and J. Granger, *PLoS One*, 2014, **9**(10), e110335.

69 A. Fihri, M. Bouhrara, B. Nekoueishahraki, J. M. Basset and V. Polshettiwar, *Chem. Soc. Rev.*, 2011, **40**, 5181–5203.

70 N. Raval, R. Maheshwari, D. Kalyane, S. R. Youngren-Ortiz, M. B. Chougule and R. K. Tekade, in *Basic Fundamentals of Drug Delivery*, Elsevier Inc., 2019, pp. 369–400.

71 J. A. Österreicher, C. Simson, A. Großalber, S. Frank and S. Gneiger, *Scr. Mater.*, 2021, **194**, 0–3.

72 L. Yu, M. Li, J. Wen, K. Amine and J. Lu, *Mater. Chem. Front.*, 2021, **5**, 5186–5193.

73 F. Wang, J. Graetz, M. S. Moreno, C. Ma, L. Wu, V. Volkov and Y. Zhu, *ACS Nano*, 2011, **5**, 1190–1197.

74 P. Zhang, B. Han, X. Yang, Y. Zou, X. Lu, X. Liu, Y. Zhu, D. Wu, S. Shen, L. Li, Y. Zhao, J. S. Francisco and M. Gu, *J. Am. Chem. Soc.*, 2022, **144**, 2129–2136.

75 K. Nishikawa and K. Shinoda, *J. Phys. Chem. Lett.*, 2021, **12**, 3922–3927.

76 J. Lang, L. Qi, Y. Luo and H. Wu, *Energy Storage Mater.*, 2017, **7**, 115–129.

77 J. R. Rodriguez, M. Flores, B. Trujillo, J. N. Díaz de León, S. B. Aguirre, R. D. Cadena-Nava, R. M. Félix, D. Sauceda and S. Camacho, *J. Colloid Interface Sci.*, 2024, **657**, 953–959.

78 A. Kondori, M. Esmaeilirad, A. M. Harzandi, R. Amine, M. T. Saray, L. Yu, T. Liu, J. Wen, N. Shan, H. H. Wang, A. T. Ngo, P. C. Redfern, C. S. Johnson, K. Amine, R. Shahbazian-Yassar, L. A. Curtiss and M. Asadi, *Science*, 2023, **379**, 499–505.

79 B. K. Spoorthi, K. Debnath, P. Basuri, A. Nagar, U. V. Waghmare and T. Pradeep, *Science*, 2024, **384**, 1012–1017.

80 H. Nie, Z. Wei, L. Qiu, X. Chen, D. T. Holden and R. G. Cooks, *Chem. Sci.*, 2020, **11**, 2356–2361.